CHEMISTRY OF MATERIALS

pubs.acs.org/cm

Article

# A′−B Intersite Cooperation-Enhanced Water Splitting in Quadruple Perovskite Oxide $CaCu_3Ir_4O_{12}$

Xubin Ye, Sanzhao Song, Lili Li, Yu-Chung Chang, Shijun Qin, Zhehong Liu, Yu-Cheng Huang, Jing Zhou, Lin-juan Zhang, Chung-Li Dong, Chih-Wen Pao, Hong-Ji Lin, Chien-Te Chen, Zhiwei Hu,* Jian-Qiang Wang,* and Youwen Long*

Cite This: *Chem. Mater.* 2021, 33, 9295−9305

Read Online

ACCESS | Metrics & More | Article Recommendations | Supporting Information

**ABSTRACT:** Developing highly efficient electrochemical catalysts and exploring the basic mechanisms for the oxygen evolution reaction (OER) are key issues for the large-scale commercialization of environmentally friendly electrolytic hydrogen energy. Compared with a simple $ABO_3$ perovskite, the *A*-site-ordered quadruple structure $AA'_3B_4O_{12}$ shows enhanced OER activity, but the underlying mechanisms remain unknown. Herein, we find that the quadruple perovskite oxide $CaCu_3Ir_4O_{12}$ has stable and superior electrochemical activity with a very low overpotential of 252 mV to achieve the current density of 10 $mA{\cdot}cm^{-2}$ in alkaline solution. Operando X-ray absorption spectroscopy reveals that the *B*-site Ir is an OER active site with a variable valence state from the initial $Ir^{4+}$ approach to $Ir^{5+}$, while the *A*′-site Cu is inactive with a constant valence state during the OER process. Density functional theory calculations demonstrate that the *A*′−*B* intersite cooperation synergistically enhances OER activity via the corner-sharing Cu−O−Ir framework owing to the strong 3*d*−2*p*−5*d* orbital hybridizations, regardless of the inactive Cu site. In the structural constitution of $CaCu_3Ir_4O_{12}$, a small Cu−O−Ir bond angle (110.7°) forms. The special orbital symmetry as well as the delicate 3*d*−5*d* levels enhance the orbital overlap and therefore promote the charge transfer, favoring the superior OER activity of $CaCu_3Ir_4O_{12}$.

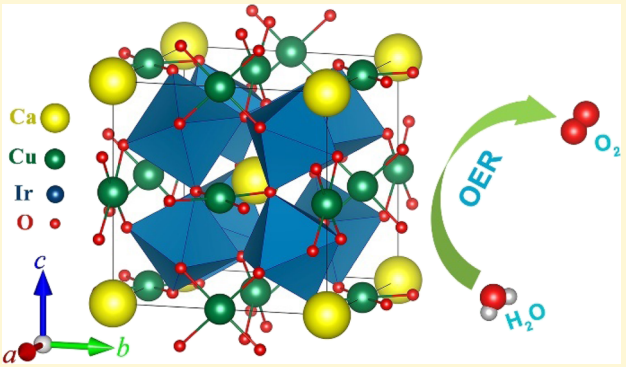


## 1. INTRODUCTION

Electrochemical water splitting powered by renewable electricity offers a promising strategy for developing a global-scale, sustainable, and fossil-free hydrogen-based energy system.[1,2] However, the scalable industrial application of water splitting remains hampered by the significant energy penalty resulting from the anodic oxygen evolution reaction because of the sluggish kinetics of the four-electron transfer process.[3] To date, most electrocatalysts such as layered double hydroxides (LDHs) (e.g., NiFe LDHs),[4] transition-metal (TM) oxides,[5] (oxy)hydroxides (e.g., FeOOH),[6] and phosphides (e.g., $Rh_2P$, $PdP_2$)[7] have specific limitations and cannot meet the large-scale commercial deployment requirements. In recent years, iridium oxide ($IrO_2$) has been widely recognized as the optimal oxygen evolution reaction (OER) catalyst. However, its high cost and low intrinsic activity greatly limit its practical applications. Therefore, the rational design of cost-effective and highly efficient electrocatalysts is an appealing research route. The design and synthesis of complex oxides show promise for reducing the content of precious metals and improving their intrinsic catalytic activity.

The perovskite oxide $ABO_3$ (*A* = alkaline, alkaline earth, or rare earth metals; *B* = TMs) has attracted extensive attention in water splitting owing to its high conductivities, structural stability, and low content of precious metals. Its high flexibility, in both ionic size and valence combinations, allows for the systematic control of electronic properties and electrochemical activities.[8,9] Partial chemical substitutions of the *A* and/or *B* sites have been exploited in many applications, leading to a series of functional properties.[10−14] For 3*d*-based perovskite catalysts, various descriptors of the OER, including orbital occupancy,[14] TM oxidation state,[15,16] and the O 2*p* band center[17] have been proposed. These descriptors imply that near-metallic, *p*−*d* hybridization, and high-valence behaviors are conducive to enhancing the electrochemical activity. However, in most cases, these features tend to significantly decrease the catalyst stability. The quadruple perovskite oxide $AA'_3B_4O_{12}$ (Figure 1a,b), where three-quarters of the *A* sites are usually occupied by Jahn−Teller active $Cu^{2+}$/$Mn^{3+}$ ions at

Received: August 31, 2021
Revised: November 14, 2021
Published: November 29, 2021

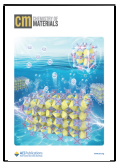

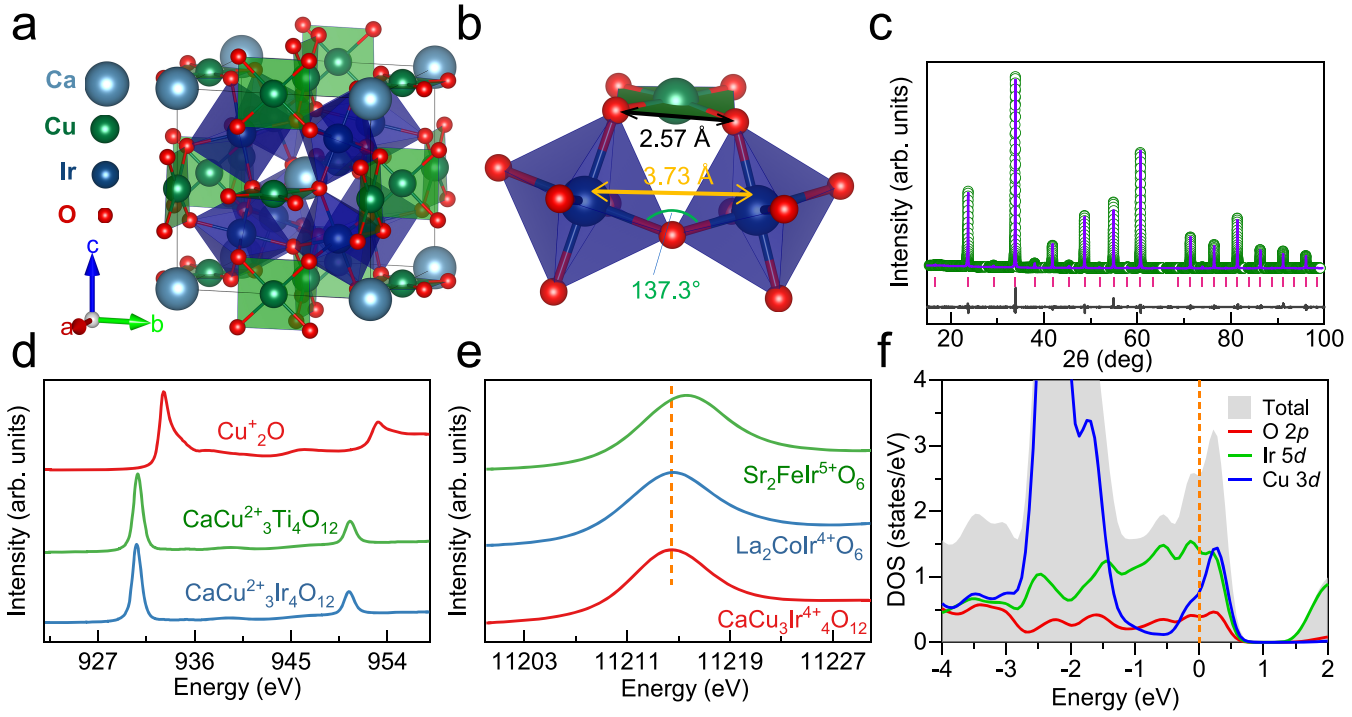


**Figure 1.** Crystal and electronic structural features of $CaCu_3Ir_4O_{12}$. (a) Schematic crystal structure of $CaCu_3Ir_4O_{12}$ with the *Im*−3 symmetry. (b) Local environment and connections of $IrO_6$ octahedra and $CuO_4$ square-planar units of $CaCu_3Ir_4O_{12}$, corresponding to the inside of the yellow circle in (a). (c) XRD pattern collected at room temperature and the corresponding Rietveld refinement results for $CaCu_3Ir_4O_{12}$. (d) XAS spectra of Cu $L_{2,3}$-edges for $CaCu_3Ir_4O_{12}$ (light blue) with related references $Cu_2O$ and $CaCu_3Ti_4O_{12}$. (e) XAS spectra of the Ir $L_3$-edge for $CaCu_3Ir_4O_{12}$ (red) with related references $La_2CoIrO_6$ and $Sr_2FeIrO_6$ as standard $Ir^{4+}$ and $Ir^{5+}$, respectively. (f) First-principles numerical results for the partial density of states near the Fermi level of $CaCu_3Ir_4O_{12}$.

the *A*' sites, shows greater activity and stability for the OER than the simple perovskite.[18−20] For example, in $CaCu_3Fe_4O_{12}$,[18] the covalent bonding network of multiple TM ions significantly enhances the structural stability. Yamada et al.[20] confirmed that the structural features of the quadruple perovskite can improve the inherent OER catalytic activity in $AMn_7O_{12}$ (i.e., $AMn_3Mn_4O_{12}$), where the small *B*−O−*B* bond angles (<140°) arising from the highly tilted $BO_6$ octahedra strongly facilitate the direct approach of adsorbates on neighboring *B* sites. However, these catalysts are still far from practical applicability because of their poor stability. By comparing the experimentally measured and theoretically calculated volcano relationships for OER,[3] Ir-based systems show promise as water-splitting electrocatalysts because they sit very near the vertex of both volcanoes (Sabatier principle). Although substantial progress has been achieved over the past decade, the fabrication of an Ir catalyst with adequate mass activity and stability remains a long-term goal impeded by the elusive nature of active sites and the poor reconstruction under working conditions. Considering the advantages of both the *A*-site-ordered quadruple perovskite structure and Ir-based systems for high catalytic performance, in this work, we report an efficient and durable $CaCu_3Ir_4O_{12}$ electrocatalyst for water splitting in an alkaline electrolyte. This oxide has the highest OER performance in Ir-based compounds. At the atomic level, operando X-ray absorption near-edge structure (XANES) and extended X-ray absorption fine-structure (EXAFS) spectroscopy investigations confirm that the optimum binding energies are induced by the unique electronic states and coordination environments of the Ir sites. Density functional theory (DFT) calculations demonstrate that the specific *A*'−*B* intersite Cu−O−Ir bonding forms a delicate energy balance; these results explicitly expatiate the synergistic effects between the *A*'-site Cu and *B*-site Ir ions that effectively boost the chemical reaction in the ordered system.[21,22]

## 2. RESULTS AND DISCUSSION

Detailed experimental and theoretical calculation methods are described in the Section 4. Powder X-ray diffraction (XRD) was used to determine the crystalline quality of the catalyst. The XRD pattern and the corresponding Rietveld analysis of $CaCu_3Ir_4O_{12}$, as shown in Figure 1c, confirm that the compound crystallizes into an *A*-site-ordered perovskite structure with space group *Im*-3. In this symmetry, Ca and Cu atoms are distributed in an orderly fashion and a 1:3 ratio at the *A* site. The detailed parameters are listed in Tables S1 and S2 of the Supporting Information. The Ir−O−Ir and Cu−O−Ir bond angles are determined to be 137.3 and 110.7°, which narrow the O−O and Ir−Ir distances to 2.57 and 3.73 Å (see Figure 1b), respectively. Owing to the strong Jahn−Teller effect of $Cu^{2+}$ (the determination of the valence state is shown later), the originally 12-fold coordination of the *A* site is distorted into square-planar $CuO_4$ units at the *A*' site, which simultaneously causes heavy tilting of the $IrO_6$ octahedra (∠Ir−O−Ir = 137.3°). The local connections of Cu−O−Ir bonds are shown in Figure 1b. Notably, the $IrO_6$ octahedra and $CuO_4$ planar units share O atoms at their corners.

Transmission electron microscopy (TEM) analysis showed that the particle size of $CaCu_3Ir_4O_{12}$ was mainly in the range 20−40 nm (Figure S1), and the elemental distribution was homogenous without visible elemental enrichment (Figure S2). The oxidation states of the Cu and Ir ions in $CaCu_3Ir_4O_{12}$


https://doi.org/10.1021/acs.chemmater.1c03015
Chem. Mater. 2021, 33, 9295−9305

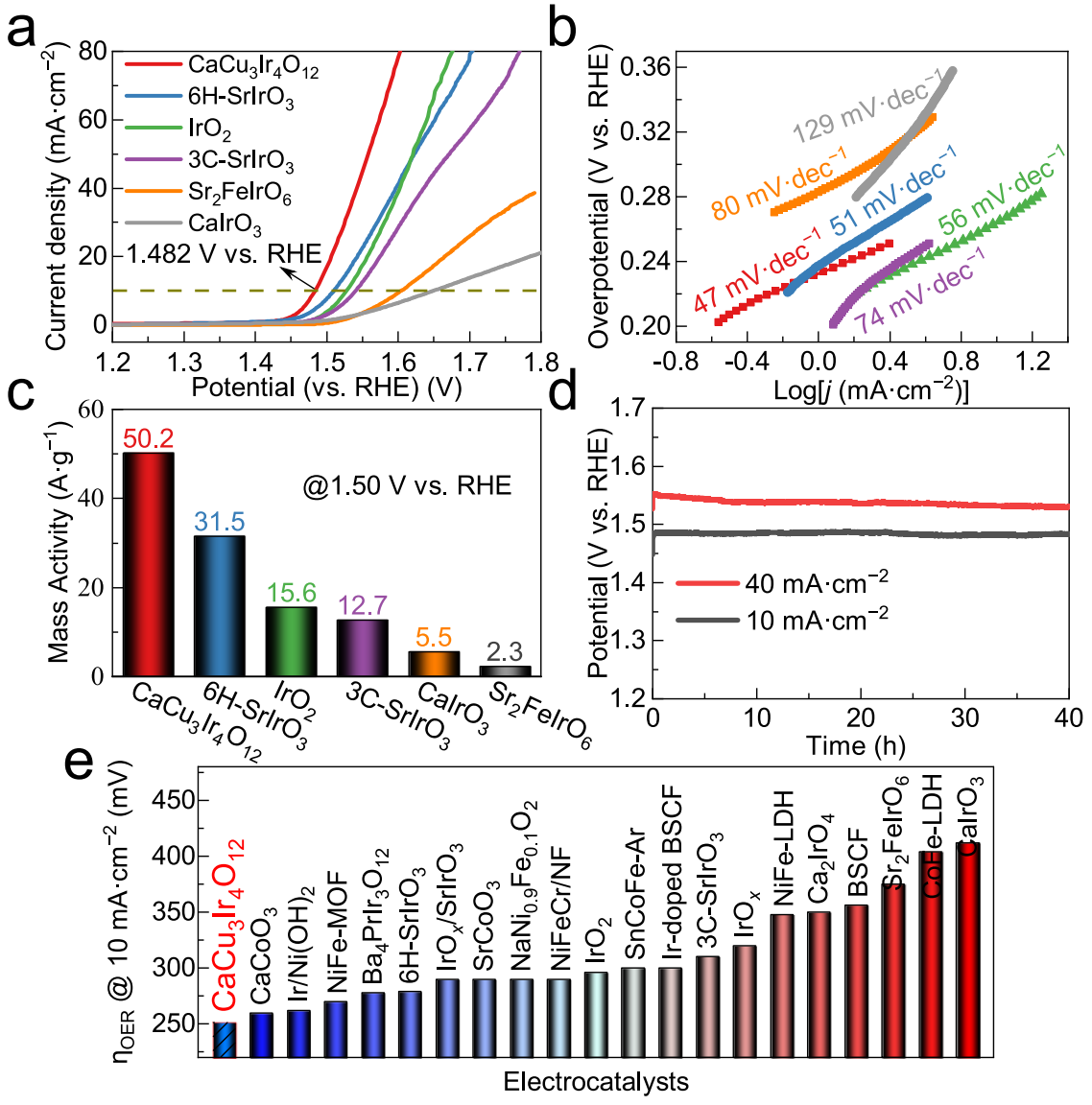


**Figure 2.** Electrocatalytic OER performance of $CaCu_3Ir_4O_{12}$. (a) OER polarization curves of $CaCu_3Ir_4O_{12}$ and references 6H-$SrIrO_3$, 3C-$SrIrO_3$, $Sr_2FeIrO_6$, $CaIrO_3$ (perovskite-type), and commercial $IrO_2$ acquired at a sweep rate of 5 mV·s$^{-1}$ in $O_2$-saturated 1 M KOH. (b) Corresponding Tafel plots. (c) Mass activity of $CaCu_3Ir_4O_{12}$ and references at 1.50 V vs RHE. (d) Chronopotentiometry measurements of $CaCu_3Ir_4O_{12}$ under the OER condition at 10 and 40 mA·cm$^{-2}$. (e) Comparison of overpotential $\eta_{OER}$ at 10 mA·cm$^{-2}$ for $CaCu_3Ir_4O_{12}$ and recently reported OER catalysts in alkaline media.

were investigated by X-ray absorption spectroscopy (XAS) at the Cu $L_{2,3}$ and Ir $L_3$ edges. Figure 1d shows the Cu $L_{2,3}$ XAS of $CaCu_3Ir_4O_{12}$ together with those of $Cu_2O$ as a $Cu^+$ ($3d^{10}$) and $CaCu_3Ti_4O_{12}$ as a $Cu^{2+}$ ($3d^9$) reference.[23−25] The Cu $L_{2,3}$ spectrum of $CaCu_3Ir_4O_{12}$ exhibits a high-intensity single peak at the same energy position as that in the spectrum of $CaCu_3Ti_4O_{12}$, revealing the formation of a $Cu^{2+}$ valence state in $CaCu_3Ir_4O_{12}$. The oxidation states of 5*d* elements can also be determined by the $L_3$ edge.[25−28] The Ir $L_3$ XAS spectrum of $CaCu_3Ir_4O_{12}$ using $La_2CoIrO_6$ as an $Ir^{4+}$ reference and $Sr_2FeIrO_6$ as an $Ir^{5+}$ reference is shown in Figure 1e. The Ir $L_3$-edge of $CaCu_3Ir_4O_{12}$ shifts to a lower energy than that of the $Ir^{5+}$ reference $Sr_2FeIrO_6$ by more than 1 eV, but coincides with the edge energy of the $Ir^{4+}$ reference $La_2CoIrO_6$, indicating the formation of the $Ir^{4+}$ valence state. The charge combination was thus confirmed to be $CaCu^{2+}{}_3Ir^{4+}{}_4O_{12}$.

Figure 1f shows the partial (per atom) density of states of $CaCu_3Ir_4O_{12}$ based on DFT calculations. The Cu 3*d*, O 2*p*, and Ir 5*d* electrons all cross the Fermi level, indicating strong 3*d*−2*p*−5*d* hybridization, in agreement with the metallic electric transport behavior (Figure S3).[29,30] This indicates that significant covalent bonding exists among the Cu 3*d*, Ir 5*d*, and O 2*p* orbitals (from −4 to 0.5 eV), which may optimize the binding energies of hydrogen and oxygen intermediates and therefore enhance the catalytic performance toward water splitting.

Inspired by the unique crystal and electronic structural features of $CaCu_3Ir_4O_{12}$, we evaluated its electrocatalytic performance for the OER. For comparison, commercial $IrO_2$, as well as homemade $CaIrO_3$, 6H-$SIrO_3$, 3C-$SrIrO_3$, and $Sr_2FeIrO_6$ were adopted as benchmarks under the same measurement conditions. Figure 2a shows the OER polarization curves measured by typical linear sweep voltammetry (LSV) for these compounds. The potential of $CaCu_3Ir_4O_{12}$ at a current density of 10 mA·cm$^{-2}$ is 1.482 V vs a reversible hydrogen electrode (RHE), which is much smaller than those


https://doi.org/10.1021/acs.chemmater.1c03015
Chem. Mater. 2021, 33, 9295−9305

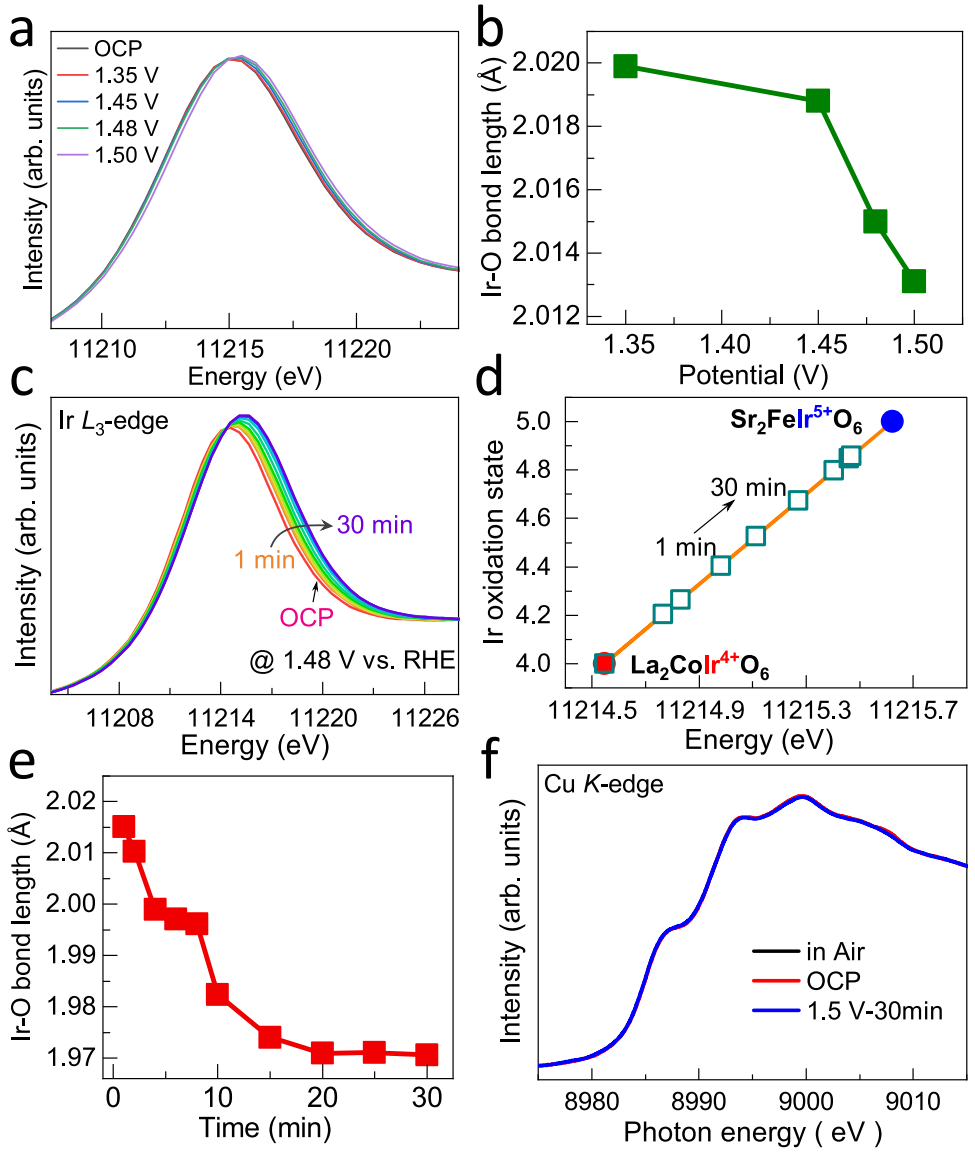


**Figure 3.** Operando spectroscopic characterization of $CaCu_3Ir_4O_{12}$. (a) Normalized operando Ir $L_3$-edge XANES spectra with various potentials in 1 M KOH at ambient conditions. OCP = open circuit potential. (b) Potential dependence of the Ir−O bond length obtained from Fourier-transform (FT) EXAFS spectra. (c) Time-dependent operando Ir $L_3$-edge XAS spectra for $CaCu_3Ir_4O_{12}$. (d) Oxidation states, derived from (c), determined by standard $Ir^{4+}$ and $Ir^{5+}$ references of $La_2CoIrO_6$ and $Sr_2FeIrO_6$, respectively. (e) Time-dependent Ir−O bond length obtained from FT-EXAFS spectra. (f) Operando Cu $K$-edge XANES spectra of $CaCu_3Ir_4O_{12}$ under various conditions.

of $IrO_2$ (1.526 V vs RHE), 6H-$SrIrO_3$ (1.509 V vs RHE), 3C-$SrIrO_3$ (1.540 V vs RHE), $CaIrO_3$ (1.642 V vs RHE), and $Sr_2FeIrO_6$ (1.605 V vs RHE). The OER current density normalized by the electrochemically active surface area (ECSA), as derived from the electrochemical double-layer capacitance measurements, was used to evaluate the number of active sites of the catalyst. Figures S4 and S5 shows the ECSA analyses of the $CaCu_3Ir_4O_{12}$, $IrO_2$, 6H-$SIrO_3$, 3C-$SrIrO_3$, and $Sr_2FeIrO_6$ catalysts. The linear slope is equivalent to the double-layer capacitance. $CaCu_3Ir_4O_{12}$ shows a larger capacitance (8.53 mF·cm$^{-2}$) than that of other catalysts, 7.65, 5.97, 5.18, and 4.51 mF·cm$^{-2}$ for 6H-$SIrO_3$, 3C-$SrIrO_3$, $IrO_2$, and $Sr_2FeIrO_6$, respectively, indicating the considerably enhanced catalytic performance in $CaCu_3Ir_4O_{12}$. In addition, Tafel plots were recorded to assess the reaction kinetics. Figure 2b shows the corresponding Tafel plots. The derived Tafel slope of $CaCu_3Ir_4O_{12}$ is only 47 mV·dec$^{-1}$. This value is smaller than those of $CaIrO_3$ (272 mV·dec$^{-1}$), $Sr_2FeIrO_6$ (80 mV·dec$^{-1}$), 3C-$SrIrO_3$ (74 mV·dec$^{-1}$), 6H-$SrIrO_3$ (51 mV·dec$^{-1}$), and $IrO_2$ (56 mV·dec$^{-1}$). Furthermore, by normalizing the current density to the catalyst mass, as shown in Figures 2c and S6, the mass activity is shown to increase sharply from 2.3−31.5 A·g$^{-1}$ in the five reference materials to 50.2 A·g$^{-1}$ in $CaCu_3Ir_4O_{12}$. All the results illustrate that the peculiar crystal and electronic structures of $CaCu_3Ir_4O_{12}$ are optimized to effectively accelerate the OER kinetics. Figure 2e summarizes the overpotential $\eta_{OER}$ at 10 mA·cm$^{-2}$ among recently reported excellent OER catalysts in alkaline media.[13,31−41] $CaCu_3Ir_4O_{12}$ presents an ultralow overpotential of 252 mV at 10 mA·cm$^{-2}$, exhibiting the highest performance among Ir-based oxide catalysts.[18−20,42−45]

To evaluate the electrochemical stability of the highly efficient $CaCu_3Ir_4O_{12}$, we probed the long-term durability via chronopotentiometry at the constant current densities of 10


https://doi.org/10.1021/acs.chemmater.1c03015
Chem. Mater. 2021, 33, 9295−9305

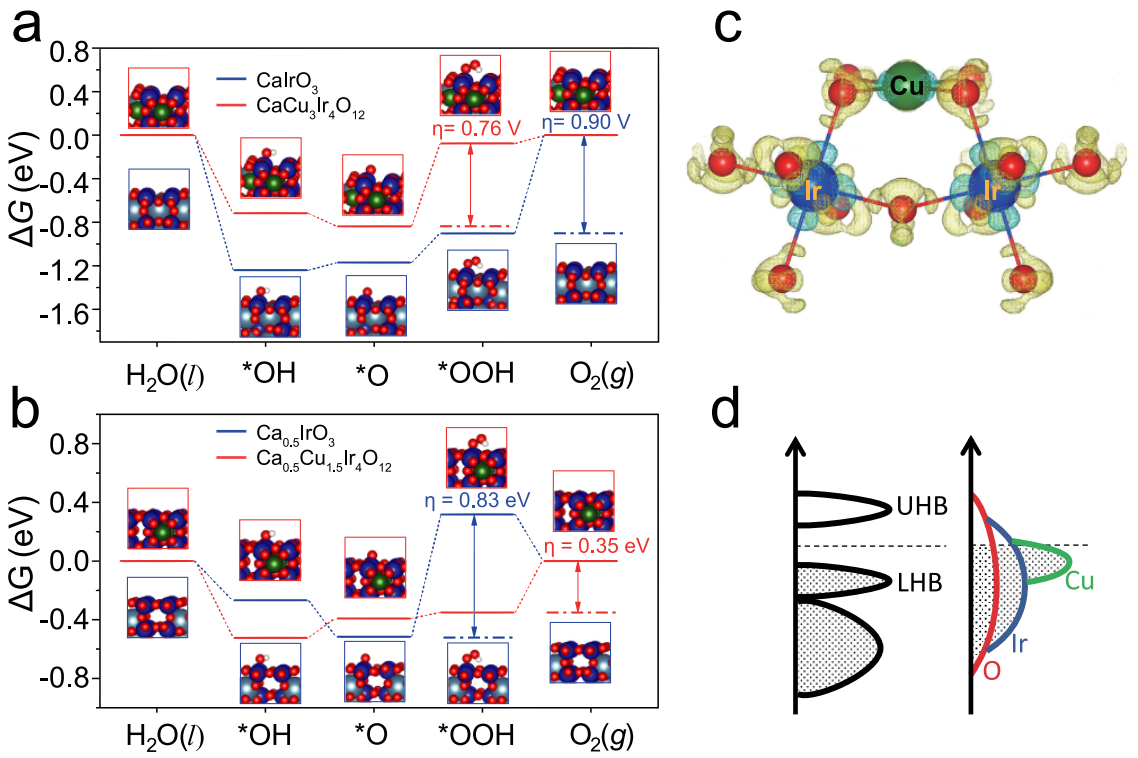


**Figure 4.** Schematic OER mechanisms involving four concerted proton−electron transfer steps in the metal-site adsorbate evolution (MAE) mechanism. (a, b) Free energies at $U_{RHE}$ = 1.23 V for concerted proton−electron transfer OER steps: (a) For the Ir site based on the MAE mechanism for $CaIr^{4+}O_3$ and $CaCu_3Ir_4{}^{4+}O_{12}$. (b) For the Ir site of $Ca_{0.5}Ir^{5+}O_3$ and $Ca_{0.5}Cu_{1.5}Ir^{5+}{}_4O_{12}$. Light blue, blue, dark green, red, and white balls represent Ca, Ir, Cu, O, and H atoms, respectively. (c) Charge density difference of the Cu−O−Ir framework in $CaCu_3Ir_4O_{12}$; blue and yellow regions represent the regions of electron depletion and accumulation, respectively. (d) Schematic band structures of $CaIrO_3$ (left) and $CaCu_3Ir_4O_{12}$ (right).

and 40 mA·cm$^{-2}$ in an alkaline solution. Figure 2d shows the chronopotentiometry curves of $CaCu_3Ir_4O_{12}$. Obviously, the real-time potential remains nearly constant with continuous operation reaching 40 h. Moreover, after the continuous long-term OER operation, the crystal structure of the electrocatalyst powder $CaCu_3Ir_4O_{12}$ was found to be unchanged, as shown by the XRD patterns (Figure S7). In addition, high-resolution TEM images show no visible variation in surface amorphization (Figure S8). Inductively coupled plasma optical emission spectroscopy (ICP-OES) measurements (Table S3) reveal that less than 6.17% Ca, 7.45% Cu, and 0.037% Ir ions are found to be dissolved in the electrolyte, indicating just a slight dissolution of metals during the OER operation. These measurements demonstrate that the crystalline phase of $CaCu_3Ir_4O_{12}$ is well preserved during the water-splitting reaction, confirming the high stability of the catalyst. Compared to other quadruple perovskite catalysts such as $CaCu_3Fe_4O_{12}$ and $AMn_7O_{12}$, the present $CaCu_3Ir_4O_{12}$ exhibits a significant improvement in stability. It is worth mentioning that in addition to the OER, $CaCu_3Ir_4O_{12}$ also displays remarkable hydrogen evolution reaction (HER) activity, superior to that of $IrO_2$ in an alkaline electrolyte. The detailed HER properties of $CaCu_3Ir_4O_{12}$ can be found in the Supporting Information (Figures S9−11 and Table S4).

To elucidate the origin of the outstanding catalytic performance of $CaCu_3Ir_4O_{12}$, the dynamic variations in the oxidation state and local coordination environment at OER-relevant potentials and times were probed by operando XANES and EXAFS.[46−49] Figures 3a and S12 show the in situ XANES profiles for the Ir $L_3$-edge as the applied potential was stepped from the open-circuit potential (OCP) to 1.50 V vs RHE. A pronounced upshift of the peak energy was observed, suggesting the formation of a more catalytically active type of Ir with a higher valence state (>$Ir^{4+}$) during the OER process. This observation reveals that the *B*-site Ir ions are active toward OER. FT $k^2$-weighted Ir $L_3$-edge EXAFS analysis was used to reveal the distortion of the local geometric structure around the Ir shell sites. The spectra at various applied potentials with corresponding fitting results and obtained structural parameters are displayed in Figure S13 and Table S5, respectively. The shrinkage of the Ir−O bond length shown in Figure 3b is observed with bias stepping to higher potentials, which can be ascribed to the shrinkage of the Ir−O bond length (Figure 3b) that is observed with bias stepping to higher potentials, which can be ascribed to the shorter effective radii of the Ir sites in the over-oxidation states. To further confirm the active site of Ir, time-dependent XANES analysis of the Ir $L_3$-edge was performed. As presented in Figure 3c, under prolonged measurement times, a trend of higher white-line energy position and intensity is clear, suggesting an increase in the valence state of Ir. Accordingly, the time dependence of the oxidation state of Ir was determined using the standard $Ir^{4+}$ and $Ir^{5+}$ references of $La_2CoIrO_6$ and $Sr_2FeIrO_6$, respectively. As illustrated in Figure 3d, the valence state of Ir gradually increased from the initial $Ir^{4+}$ to an average $Ir^{4.83+}$ state within 30 min. Time-dependent operando FT-EXAFS analyses were also performed. The spectra with corresponding fitting results are shown in Figures S14−15 and Table S6. The center of the peaks gradually moved to the left (Figure S14), indicating that the Ir−O bond


https://doi.org/10.1021/acs.chemmater.1c03015
Chem. Mater. 2021, 33, 9295−9305

length was slightly decreased with the reaction time, as shown in Figure 3e. These results reveal the formation of oxo-ligands and a larger number of 5*d*-band holes for surficial Ir sites during the OER. As reported elsewhere,[50,51] the increasing number of Ir 5*d* vacancies and the shrinking Ir−O ligands could lead to the formation of O 2*p* holes. The electron-deficient intermediate O species would appear as terminal ligands, which can be considered as one of the key factors for the enhanced catalytic reactivity for OER in our $CaCu_3Ir_4O_{12}$ catalyst. The operando Cu *K*-edge XANES spectra are shown in Figure 3f. In sharp contrast to the Ir $L_3$-edge XANES, no visible time or potential dependence appears, indicating that the *A*'-site Cu is not an active site.

Based on first-principles theoretical calculations, we investigated the synergistic effects of Cu 3*d*, O 2*p*, and Ir 5*d* hybridization in $CaCu_3Ir_4O_{12}$ by considering *B*-site Ir as the OER active site. Here, the crystal (001) plane terminated with Ir and O atoms was adopted to model the surface reaction pathways, and the metal-site adsorbate evolution mechanism scenario was considered as the reaction mechanism, involving four consecutive proton−electron transfer steps with *OH, *O, and *OOH intermediates.[52] We first constructed Ir ions with the same valence in both $CaIr^{4+}O_3$ and $CaCu_3Ir^{4+}{}_4O_{12}$ (Figure S16); the only difference between these two systems is the presence or absence of Cu 3*d* orbitals at the *A*' site, which participate in the bonding with the O 2*p* orbitals. Figure 4a shows the Gibbs free energy ($\Delta G$) diagrams under $U_{RHE}$ = 1.23 V of $CaIr^{4+}O_3$ and $CaCu_3Ir^{4+}{}_4O_{12}$ obtained from the metal-site adsorbate evolution mechanisms. For the two samples, the first step of the reaction of *OH formation occurs spontaneously because of the negative energy difference; the second step of *O formation occurs with very small energy fluctuations. Moreover, for $CaIr^{4+}O_3$, the free energy of the *OH intermediate is minimal, indicating high binding strength. The $\Delta G$ difference between the *OOH intermediate and $O_2(g)$ is maximized, indicating that the rate-determining step is the formation of $O_2(g)$, which results in a high OER overpotential of 0.90 V. It has been reported that optimal catalysts must have bond strengths that are neither too high nor too low. The high theoretical potentials in $CaIr^{4+}O_3$ are attributed to the strong adsorption capacity of the *OH intermediates. For $CaCu_3Ir^{4+}{}_4O_{12}$, the free energy consumption of *OOH formation ($\Delta G_{*OOH} - \Delta G_{*O}$ = 0.76 eV) was found to be maximized. This is lower than that for the same valence of Ir as the active site in $CaIr^{4+}O_3$ without *A*'-site Cu. This DFT calculation demonstrates that the OER activity of the Ir site can be enhanced through Cu 3*d* participation. Furthermore, we constructed a $Ca_{0.5}Cu_{1.5}Ir^{5+}{}_4O_{12}$ system with 50% Ca and Cu leaching from $CaCu_3Ir_4O_{12}$, as observed from operando Ir $L_3$ XANES. $Ca_{0.5}Ir^{5+}O_3$ with the same Ir valence was also considered. As shown in Figure 4b, for $Ca_{0.5}Cu_{1.5}Ir^{5+}{}_4O_{12}$, the energy difference of *OOH formation is greatly reduced, and the rate-determining step is the formation of $O_2(g)$. The opposite is true for $Ca_{0.5}Ir^{5+}O_3$. Compared to the two $Ir^{4+}$ systems mentioned above, the overpotentials for $Ca_{0.5}Ir^{5+}O_3$ and $Ca_{0.5}Cu_{1.5}Ir^{5+}{}_4O_{12}$ are decreased to 0.83 and 0.35 V, respectively. This reveals the important role of high-valence Ir participation in enhancing OER activity and indicates that the lattice oxygen could be further activated by 3*d* participation in covalent bonding. Thus, our theoretical results prove that the OER activity can be synergistically enhanced through a strong Cu 3*d*−O 2*p*−Ir 5*d* covalent mixture. This finding was also confirmed by the simulation of the charge density. The charge density difference was calculated based on $\rho(r) = \rho(CaCu_3Ir_4O_{12}, r) - \sum\rho(X, r)$, where $\rho(X, r)$ represents the atomic charge distribution of the corresponding single atom *X* in $CaCu_3Ir_4O_{12}$. The covalent bonding behavior can be observed along with the Cu−O−Ir pathway. As shown in Figure 4c, the O atoms, which are connected to the $IrO_6$ and $CuO_4$ units, display strong orbital hybridizations with those of the Cu 3*d* and Ir 5*d* electrons. The Cu−O−Ir covalent framework could provide robustness to the catalyst during the water-splitting process. In water splitting, the valence state of Ir approached +5. This suggested that the electron density around Ir was decreased with the attachment of the adsorbate to the active Ir site. Thus, a slight fluctuation of the electron cloud is likely to occur in the strongly hybridized Cu−O−Ir framework in this reaction, without requiring a change in the valence state of Cu. This subtle energy regulation enables the catalytic process to facilitate adsorption and desorption.

The unique crystal and electronic structures of $CaCu_3Ir_4O_{12}$ lead to its outstanding catalytic performance. In the crystal structure, the introduction of $Cu^{2+}$ at the *A*' site causes heavy $IrO_6$ octahedral tilting at the *B* site, which significantly reduces the Ir−Ir and O−O bond lengths. $CaCu_3Ir_4O_{12}$ shows the smallest Ir−O−Ir bond angle (137.3°) and the shortest Ir−Ir distance (3.73 Å) among the reported Ir-based perovskite oxides with corner-sharing $IrO_6$ octahedra. In addition, the small Cu−O−Ir bond angle (110.7°) is rare among the reported double perovskites, where the average Cu−O−Ir bond angle, for example, is close to 152° in $La_2CuIrO_6$.[53] This yields a special interaction between Cu and Ir. These features are far beyond what can be achieved by chemical doping in simple perovskites. In the OER process, the contact direction between the adsorbate and the catalyst lattice, and the distances between the adsorbate on one active site and those on adjacent active sites and the adjacent active sites all change significantly. The effects of the surrounding environment may cause changes in the catalytic mechanism, as proposed for $AMn_3Mn_4O_{12}$ and $CaCu_3Fe_4O_{12}$.[18,20] The electronic band structure determines the electrical conductivity as well as the charge-transfer efficiency, which can affect the catalytic performance. Figure 4d illustrates the schematic band structures of two classes of essentially different $Ir^{4+}$ electronic states for $CaIrO_3$ and $CaCu_3Ir_4O_{12}$. It is well known that in perovskite-like materials with the $Ir^{4+}$ ($5d^5$) electron configuration,[54] the Ir−5*d* states are split into the fully occupied lower Hubbard band and the empty upper Hubbard band, corresponding to the Mott insulating behavior (see the left side of Figure 4d), as observed in $CaIrO_3$ and $Ca_2IrO_4$.[55−57] However, in $CaCu_3Ir_4O_{12}$, as shown in the right side of Figure 4d, the participation of Cu-3*d* induces strong bonding with the O 2*p* and Ir 5*d* states. All of these orbitals cross the Fermi level, suggesting that the strongly hybridized Cu−O−Ir bonds form a covalent network and therefore reinforce the electric transport.[29] As a result, $CaCu_3Ir_4O_{12}$ exhibits metallic conducting behavior (Figure S3). Its resistivity is approximately one order lower than that of $IrO_2$. To gain a deeper understanding, a systematic comparison of both catalytic activity and conductivity was performed for several $Ir^{4+}$-based compounds (Figures S17−19). Compared to the poor catalytic activities of the insulating $CaIrO_3$, $Ca_2IrO_4$, $Sr_2FeIrO_6$ and $La_2CuIrO_6$,[37,53] the metallic $IrO_2$ shows significantly better performance for water splitting, which is further enhanced in $CaCu_3Ir_4O_{12}$. These results agree well with


https://doi.org/10.1021/acs.chemmater.1c03015
Chem. Mater. 2021, 33, 9295−9305

the fact that a higher electrical conductivity favors catalytic activity because metallicity can ensure faster charge transfer at both the catalyst−electrolyte and catalyst−support electrode interfaces.[58,59] In addition, although the same TM ions of $Cu^{2+}$ and $Ir^{4+}$ are present in $CaCu_3Ir_4O_{12}$ and $La_2CuIrO_6$, these two materials have completely different properties. $La_2CuIrO_6$ is an insulator with very poor chemical activity. This fundamental difference from the properties of $CaCu_3Ir_4O_{12}$ is related to the $Cu^{2+}$−$Ir^{4+}$ ordering patterns. In the double perovskite $La_2CuIrO_6$, $Cu^{2+}$ and $Ir^{4+}$ are arranged in a rock-salt type cation ordering, where the Cu−O−Ir bond angles are larger than 140° and can approach 180°. In this case, electron hopping between, for example, orbitals at two lattice sites has a higher energy barrier because of the larger crystal field splitting energy on 5*d* electrons,[60,61] and hopping between $t_{2g}$ and, for example, orbitals is prohibited by the orbital symmetry.[62,63] However, in $CaCu_3Ir_4O_{12}$, the small bond angle (110.7°) is closer to that of the 90° model. Electron hopping between $Cu^{2+}$ and $Ir^{4+}$ via oxygen is allowed on both the orbital symmetry and energy levels. From this perspective, $CaCu_3Ir_4O_{12}$ has a unique crystal structure and electronic structure, which allows compensation for the shortcomings of simple and double perovskites. Therefore, *A*'−*B* intersite cooperation can significantly enhance the catalytic performance of $CaCu_3Ir_4O_{12}$.

## 3. CONCLUSIONS

In conclusion, we developed the quadruple perovskite iridate oxide $CaCu_3Ir_4O_{12}$ as a superior OER catalyst with high activity and excellent stability for alkaline water oxidation. At 10 mA·cm$^{-2}$, the catalyst presented a potential of 1.482 V vs RHE, corresponding to an ultralow overpotential of 252 mV and a low Tafel slope of 57 eV·dec$^{-1}$. The mass activity reaches 50.2 A·g$^{-1}$ at 1.50 V, which is over three times higher than that of the state-of-the-art $IrO_2$. In addition, much better durability, up to 40 h, was also exhibited by this compound. These observations show that the current $CaCu_3Ir_4O_{12}$ exhibits the highest performance among Ir-based oxide catalysts and appreciable stability for OER. Moreover, operando XANES analysis revealed that the valence state of Ir was gradually increased from the initial $Ir^{4+}$ to an average $Ir^{4.83+}$ state, indicating that Ir is the active site, while the *A*'-site Cu is not an active site in the water-splitting process. DFT calculations and electronic structure studies revealed that the introduction of $Cu^{2+}$ promoted the optimal crystal structure and the resulting electronic structure and that the Cu−O−Ir covalent framework improved the catalytic performance. Therefore, the proposed strategy is to synthesize mixed or complex oxides containing multiple TM, in which noble metals are partially replaced by earth-abundant elements. This helps achieve balance among the activity, stability, and cost of the OER catalysts. Our results not only demonstrate that quadruple perovskite oxides hold great potential for alkaline water oxidation but also clarify the underlying catalytic mechanisms for the first time, providing a guide for designing superior catalysts from materials with complex structures.

## 4. EXPERIMENTAL SECTION

**4.1. Synthesis of the Catalyst.** The polycrystalline $CaCu_3Ir_4O_{12}$ was synthesized using high-temperature and high-pressure (HPHT) methods. Highly pure $CaCO_3$, CuO, and Ir powder were used as starting materials. These reagents were thoroughly mixed at a 1:3:4 mole ratio in an agate mortar and sintered using the conventional solid-state reaction at 1273 K for 24 h in air. Then, the obtained precursor was sealed into a gold capsule with 3.0 mm in diameter and length. The capsule was treated at 9 GPa and 1523 K for 30 min on a cubic anvil-type high-pressure apparatus. The sample was quenched to room temperature (RT) once the heat treatment was finished, and then, the pressure was gradually released. Perovskite-type $CaIrO_3$ was synthesized using a similar HPHT process. A powder mixture of CaO and $IrO_2$ with a molar ratio of 1:1 was used as the starting material. CaO was obtained by firing $CaCO_3$ at 1273 K for 10 h in air. The HPHT treatment was performed under 2 GPa and 1773 K for 30 min.[56] Double perovskite $La_2CuIrO_6$ was synthesized using a conventional solid-state method under ambient conditions. The mixture of high-purity $La_2O_3$, CuO, and Ir powder was calcined in air at 1173 K for 3 days.

**4.2. Characterization of the Catalyst.** The sample quality and crystal structure were identified by powder XRD on a Huber diffractometer with Cu K$\alpha$1 radiation ($\lambda$ = 1.5406 Å). The diffraction angle ($2\theta$) varies from 10 to 100° with 0.005° per step. The structure refinement was performed using the Rietveld method using the general structure analysis system (GSAS) program.[64] TEM, high-resolution TEM (HRTEM), and energy-dispersive X-ray spectra (EDS) images were acquired using a transmission electron microscope of Tecani-G2 T20 and F20, which was operated with a spherical aberration corrector at an acceleration voltage of 200 kV. For TEM specimen preparation, the catalyst powders were first dispersed in ethanol by sonication and then dropped onto a carbon-coated molybdenum grid with micropipettes, followed by drying under ambient conditions. The temperature dependence of the electrical resistivity, $\rho(T)$, of the compounds was measured at the temperature range of 2−300 K using a standard four-probe method on a physical property measurement system (PPMS7, Quantum Design). Electrical contacts were formed on a bar-shaped pellet using silver paste and Au wires. The gauge current was 1 mA. Soft XAS measurements of Cu $L_{2,3}$-edges were carried out at beamline BL11A of the National Synchrotron Radiation Research Center (NSRRC) in Taiwan and BL02B in Shanghai Synchrotron Radiation Facility (SSRF) using the total electron yield mode. The ex situ Ir-$L_3$ spectra were measured at beamline BL07A of the NSRRC in the transmission geometry. The operando XANES at Ir $L_3$-edge was performed at the beamline 44A of the NSRRC. Operando XAS experiments were performed under the desired conditions with a custom-built operando XAS instrument. All XAS data were analyzed using the standard program Demeter.

**4.3. Electrochemical Measurements of OER Activities.** Electrochemical measurements were performed at RT using a rotating disk working electrode (RDE) made of glassy carbon (GC) (PINE, 5 mm diameter, 0.196 cm$^2$) connected to a PGSTAT 302 N (Metrohm Autolab) electrochemical system. The GC electrode was prepolished with different diameters of $\alpha$-$Al_2O_3$ slurries (1.0 $\mu$m, 0.3 $\mu$m, and 50 nm, orderly) on a polishing cloth and sonicated in ethanol for 5 min. The electrodes were finally rinsed with deionized water (DI water) and dried before each test. A Pt wire placed in a fritted glass tube and Hg/HgO was used as the counter and reference electrodes, respectively. All the potentials were calibrated to the RHE using the following equation: $E_{RHE} = E_{Hg/HgO} + 0.197\ V + 0.059\ pH$. The preparation method of the working electrodes containing the investigated catalysts is as follows: 5 mg of the electrocatalyst powder was dispersed in 1 mL of 3:1 (volume ratio) DI water/isopropanol mixed solvent with 40 $\mu$L of Nafion (5 wt %, Sigma-Aldrich), and then, the mixture was sonicated in an ultrasonic water bath for about 1 h. After that, 10 $\mu$L of the dispersion was dropped onto the GC disk with a diameter of 5 mm, leading to the catalyst loading of about 0.245 mg·cm$^{-2}$. Finally, the as-prepared electrode was dried at RT.

The electrolyte was 1 M KOH aqueous solution (99.99% metal purity, pH ∼ 13.8), which was saturated with $O_2$ for 30 min before each test and maintained under an $O_2$ atmosphere throughout. LSV was performed with the RDE at 1600 rpm in $O_2$-saturated 1 M KOH solution at a scan rate of 5 mV·s$^{-1}$ after the catalyst was completely activated and stabilized. All potential values are *iR*-corrected to compensate for the effect of solution resistance as the following equation: $E_{iR\text{-corrected}} = E - iR$, where *i* is the current, and *R* is the


https://doi.org/10.1021/acs.chemmater.1c03015
Chem. Mater. 2021, 33, 9295−9305

uncompensated ohmic electrolyte resistance (~4 Ω) measured via high-frequency AC impedance in $O_2$-saturated 1 M KOH. The stability tests were performed in $O_2$-saturated 1 M KOH by chronopotentiometry measurements at different current densities. The values of mass activity ($A{\cdot}g^{-1}$) were calculated from the oxide catalyst loading $m$ (0.245 $mg{\cdot}cm^{-2}$) and the measured current density $j$ ($mA{\cdot}cm^{-2}$) at overpotential $\eta$ = 270 or 180 mV using the following equation: mass activity = $j/m$. ICP-OES was performed on a Perkin-Elmer Optima 3300DV ICP spectrometer.

The ECSA of each sample was obtained by determining the double-layer capacitance at non-Faradaic potential range, according to the method reported by McCrory et al.[36] A series of cyclic voltammetry (CV) measurements were performed at various scan rates (20, 40, 60, 80, 100, and 120 $mV{\cdot}s^{-1}$) in the potential window between 1.031 and 1.13 V vs RHE. Then, a linear plot was estimated by plotting $\Delta j = (j_+ - j_-)/2$ at $(i_a - i_c)$ at 1.08 V vs RHE and the scan rate. The double-layer capacitance ($C_{dl}$) is one half of the slope value of the fitting line. The ECSA can be obtained by dividing $C_{dl}$ by the specific capacitance ($C_s$). A $C_s$ value of 0.040 $mF{\cdot}cm^{-2}$ was suggested in a previously reported work.[36]

**4.4. Computational Details.** The present calculations employed the Vienna ab initio simulation package (VASP)[65,66] implementation of DFT in conjunction with the projector augmented wave (PAW) formalism. The exchange-correlation term was modeled using the generalized gradient approximation (GGA) with Perdew–Burke–Ernzerhof (PBE).[67] Consequently, the H $1s^1$, O $2s^22p^4$, Ca $3p^64s^2$, Cu $3d^{10}5s^1$, and Ir $6s^25d^7$ states were treated as valence electrons. The electronic wave functions were expanded in plane waves using an energy cutoff of 520 eV. The Hubbard model[68] was applied to describe the strong correlation of the localized Ir 5$d$ states, and the value of $U_{eff}$ was set to 2.00 eV according to a previous work.[69] The force and energy convergence criteria were set to 0.02 $eV{\cdot}Å^{-1}$ and $10^{-5}$ eV, respectively. The 4 × 4 × 1 Monkhorst–Pack[70] $k$-point meshes were employed to sample the Brillouin zones for all calculations. To prevent spurious interactions, a vacuum spacing with a thickness of 15 Å was constructed in the $z$-direction. We calculated the Gibbs free energy differences ($\Delta G$) using the computational hydrogen electrode model under standard conditions, with the voltage applied $U_{RHE}$ = 1.23 V.

**4.5. Free Energy Calculations.** The elementary steps of metal-site adsorbate evolution mechanisms are assumed to proceed through four consecutive proton and electron-transfer steps with *OH, *O, and *OOH intermediates, as shown below:

$$H_2O(l) + * \rightarrow *OH + e^- + H^+ \quad (1)$$

$$*OH \rightarrow *O + e^- + H^+ \quad (2)$$

$$H_2O(l) + *O \rightarrow *OOH + e^- + H^+ \quad (3)$$

$$*OOH \rightarrow O_2(g) + e^- + H^+ \quad (4)$$

The *OH, *O, and *OOH represent OH, O, and OOH species adsorbed on the metal site (*) on the surface, respectively. The Gibbs free energy changes ($\Delta G$) for the water oxidation steps were calculated using the following equations:

$$\Delta G1 = \Delta G[*OH] - eU_{RHE} \quad (5)$$

$$\Delta G2 = \Delta G[*O] - \Delta G[*OH] - eU_{RHE} \quad (6)$$

$$\Delta G3 = \Delta G[*OOH] - \Delta G[*O] - eU_{RHE} \quad (7)$$

$$\Delta G4 = -2\Delta g^{exp}_{H_2O} - \Delta G[*OOH] - eU_{RHE} \quad (8)$$

$U_{RHE}$ is the potential measured against RHE at the standard condition ($T$ = 298.15 K, $P$ = 1 bar, and pH = 0), and is the experimental Gibbs free energy of the formation of water molecules. The $\Delta G$ of these intermediates includes zero-point energy (ZPE) and entropy corrections according to $\Delta G = \Delta E + \Delta ZPE - T\Delta S$, where the energy differences $\Delta E$ are calculated with respect to $H_2O(l)$ and $H_2(g)$ (at $U_{RHE}$ = 0 and pH = 0). The theoretical overpotential is defined as the lowest potential at which all reaction steps are thermodynamically downhill.

*4.5.1. HER Activity.* $CaCu_3Ir_4O_{12}$ also displays remarkable HER activity in alkaline electrolytes. The HER performances were also evaluated using the LSV curves. Figure S9a displays representative polarization curves for $CaCu_3Ir_4O_{12}$, $IrO_2$, and Pt/C, while the performance of $CaIrO_3$ is too poor to be shown. The obtained overpotential $\eta_{HER}$ at a current density of 10 $mA{\cdot}cm^{-2}$ is 187 mV for $CaCu_3Ir_4O_{12}$, 291 mV for $IrO_2$, and 65 mV for Pt/C. Impressively, although the HER performance of $CaCu_3Ir_4O_{12}$ is weaker than that of Pt/C, it displays a much higher performance compared with that of $IrO_2$. Figure S9b illustrates the corresponding Tafel plots. The resulting Tafel slopes are 39, 32, and 53 $mV{\cdot}dec^{-1}$ for $CaCu_3Ir_4O_{12}$, Pt/C, and $IrO_2$, respectively. The former two have comparable values that are considerably lower than that of $IrO_2$, indicating that the surface chemistry mechanism responsible for HER in $CaCu_3Ir_4O_{12}$ and Pt/C may be similar but different from that of $IrO_2$. Mass activities for $CaCu_3Ir_4O_{12}$, $IrO_2$, and Pt/C are illustrated in Figure S10. The value of $CaCu_3Ir_4O_{12}$ at an overpotential of 18 mV is 40.8 $A{\cdot}g^{-1}$, which is larger than that of $IrO_2$ (6.7 $A{\cdot}g^{-1}$) 6 times. The chronopotentiometry measurement was also used to evaluate the electrochemical stability of $CaCu_3Ir_4O_{12}$ under the HER condition. As shown in Figure S11, the potential can be maintained nearly unchanged during the measurement we tested. These results all further indicate that $CaCu_3Ir_4O_{12}$ has a superior HER activity and high stability. Table S4 summarizes $\eta_{HER}$ and Tafel slopes for $CaCu_3Ir_4O_{12}$ and other recently reported promising electrocatalysts under the HER condition in the alkaline electrolyte, suggesting that $CaCu_3Ir_4O_{12}$ has the potential to be a catalyst for overall water splitting.

## ■ ASSOCIATED CONTENT

### Supporting Information

The Supporting Information is available free of charge at https://pubs.acs.org/doi/10.1021/acs.chemmater.1c03015.

Particle size analysis using the TEM method; elemental mapping images; temperature-dependent resistivity measured between 2–300 K for $CaCu_3Ir_4O_{12}$ and $IrO_2$; ECSA analyses of $CaCu_3Ir_4O_{12}$, commercial $IrO_2$, 6H-$SrIrO_3$, 3C-$SrIrO_3$, and $Sr_2FeIrO_6$ catalysts; mass activity based on the oxide weight at different potentials; XRD patterns of $CaCu_3Ir_4O_{12}$ before and after OER; HRTEM images of $CaCu_3Ir_4O_{12}$ before and after OER; HER polarization curves of $CaCu_3Ir_4O_{12}$ and related references; mass activity for HER; chronopotentiometry measurement under the HER condition of $CaCu_3Ir_4O_{12}$ at 10 $mA{\cdot}cm^{-2}$; normalized operando Ir $L_3$-edge XANES spectra with various potentials; Fourier transform $k^2$-weighted Ir $L_3$-edge EXAFS spectra of $CaCu_3Ir_4O_{12}$ with reference $IrO_2$ under various potentials; 3D and color map showing the time-dependent operando FT-EXAFS spectra at the Ir $L_3$-edge of $CaCu_3Ir_4O_{12}$; Fourier transform $k^2$-weighted Ir $L_3$-edge EXAFS spectra of $CaCu_3Ir_4O_{12}$ with various times; optimized local structures for the (001) surface; systematic comparison of OER polarization curves for $CaCu_3Ir_4O_{12}$ and related references; temperature-dependent resistivity measured between 2–300 K for related insulating references; systematic comparison of catalytic activity and conductivity for $CaCu_3Ir_4O_{12}$ and related references; crystallographic parameters of $CaCu_3Ir_4O_{12}$ refined from the XRD pattern at RT; selected bond lengths and angles for $CaCu_3Ir_4O_{12}$; ICP-OES analysis for $CaCu_3Ir_4O_{12}$ after the durability test; summary of the HER performance for $CaCu_3Ir_4O_{12}$ and other state-of-



https://doi.org/10.1021/acs.chemmater.1c03015
Chem. Mater. 2021, 33, 9295–9305

the-art perovskite electrocatalysts; structural parameters of $CaCu_3Ir_4O_{12}$ and reference samples with various potentials extracted from the Ir $L_3$-edge EXAFS fitting; and structural parameters of $CaCu_3Ir_4O_{12}$ with various times extracted from the Ir $L_3$-edge EXAFS fitting (PDF)

## AUTHOR INFORMATION


### Corresponding Authors

**Zhiwei Hu** − *Max Planck Institute for Chemical Physics of Solids, Dresden 01187, Germany;* orcid.org/0000-0003-0324-2227; Email: Zhiwei.Hu@cpfs.mpg.de

**Jian-Qiang Wang** − *Key Laboratory of Interfacial Physics and Technology, Shanghai Institute of Applied Physics, Chinese Academy of Sciences, Shanghai 201800, China; University of Chinese Academy of Sciences, Beijing 100049, China;* orcid.org/0000-0003-4123-7592; Email: wangjianqiang@sinap.ac.cn

**Youwen Long** − *Beijing National Laboratory for Condensed Matter Physics, Institute of Physics, Chinese Academy of Sciences, Beijing 100190, China; University of Chinese Academy of Sciences, Beijing 100049, China; Songshan Lake Materialsa Laboratory, Dongguan 523808, China;* orcid.org/0000-0002-8587-7818; Email: ywlong@iphy.ac.cn

### Authors

**Xubin Ye** − *Beijing National Laboratory for Condensed Matter Physics, Institute of Physics, Chinese Academy of Sciences, Beijing 100190, China; University of Chinese Academy of Sciences, Beijing 100049, China;* orcid.org/0000-0002-5739-8318

**Sanzhao Song** − *Key Laboratory of Interfacial Physics and Technology, Shanghai Institute of Applied Physics, Chinese Academy of Sciences, Shanghai 201800, China*

**Lili Li** − *Key Laboratory of Interfacial Physics and Technology, Shanghai Institute of Applied Physics, Chinese Academy of Sciences, Shanghai 201800, China*

**Yu-Chung Chang** − *National Synchrotron Radiation Research Center, Hsinchu 30076, Taiwan*

**Shijun Qin** − *Beijing National Laboratory for Condensed Matter Physics, Institute of Physics, Chinese Academy of Sciences, Beijing 100190, China; University of Chinese Academy of Sciences, Beijing 100049, China*

**Zhehong Liu** − *Beijing National Laboratory for Condensed Matter Physics, Institute of Physics, Chinese Academy of Sciences, Beijing 100190, China; University of Chinese Academy of Sciences, Beijing 100049, China*

**Yu-Cheng Huang** − *Department of Physics, Tamkang University, New Taipei City 25137, Taiwan*

**Jing Zhou** − *Key Laboratory of Interfacial Physics and Technology, Shanghai Institute of Applied Physics, Chinese Academy of Sciences, Shanghai 201800, China*

**Lin-juan Zhang** − *Key Laboratory of Interfacial Physics and Technology, Shanghai Institute of Applied Physics, Chinese Academy of Sciences, Shanghai 201800, China;* orcid.org/0000-0003-4704-5807

**Chung-Li Dong** − *Department of Physics, Tamkang University, New Taipei City 25137, Taiwan;* orcid.org/0000-0002-4289-4677

**Chih-Wen Pao** − *National Synchrotron Radiation Research Center, Hsinchu 30076, Taiwan*

**Hong-Ji Lin** − *National Synchrotron Radiation Research Center, Hsinchu 30076, Taiwan*

**Chien-Te Chen** − *National Synchrotron Radiation Research Center, Hsinchu 30076, Taiwan*

Complete contact information is available at: https://pubs.acs.org/10.1021/acs.chemmater.1c03015


### Author Contributions

The manuscript was written through contributions of all authors. All authors have given approval to the final version of the manuscript. X.Y. and S.S. contributed equally.

### Notes

The authors declare no competing financial interest.

## ACKNOWLEDGMENTS

This work was supported by the National Natural Science Foundation of China (Grant No. 11934017, 51772324, and 11921004), the National Key R&D Program of China (Grant No. 2018YFE0103200, 2018YFA0305700), the Beijing Natural Science Foundation (Grant No. Z200007), the Chinese Academy of Sciences (Grant No. XDB33000000, XDA2100000, and QYZDB−SSW−SLH013), the K. C. Wong Education Foundation (Grant No. GJTD-2018-10), and the China Postdoctoral Science Foundation funded project (2020 T130676). We acknowledge the support from the Max Planck-POSTECH-Hsinchu Center for Complex Phase Materials.

## REFERENCES


(1) Chu, S.; Majumdar, A. Opportunities and Challenges for a Sustainable Energy Future. *Nature* **2012**, *488*, 294−303.

(2) Koper, M. T. M. Hydrogen Electrocatalysis a Basic Solution. *Nat. Chem.* **2013**, *5*, 255−256.

(3) Seh, Z. W.; Kibsgaard, J.; Dickens, C. F.; Chorkendorff, I. B.; Nørskov, J. K.; Jaramillo, T. F. Combining Theory and Experiment in Electrocatalysis: Insights into Materials Design. *Science* **2017**, *355*, No. eaad4998.

(4) Stevens, M. B.; Trang, C. D. M.; Enman, L. J.; Deng, J.; Boettcher, S. W. Reactive Fe-Sites in Ni/Fe (Oxy)hydroxide Are Responsible for Exceptional Oxygen Electrocatalysis Activity. *J. Am. Chem. Soc.* **2017**, *139*, 11361−11364.

(5) Wang, J.; Gao, Y.; Kong, H.; Kim, J.; Choi, S.; Ciucci, F.; Hao, Y.; Yang, S.; Shao, Z.; Lim, J. Non-Precious-Metal Catalysts for Alkaline Water Electrolysis: Operando Characterizations, Theoretical Calculations, and Recent Advances. *Chem. Soc. Rev.* **2020**, *49*, 9154−9196.

(6) Feng, C.; Faheem, M. B.; Fu, J.; Xiao, Y.; Li, C.; Li, Y. Fe-Based Electrocatalysts for Oxygen Evolution Reaction: Progress and Perspectives. *ACS Catal.* **2020**, *10*, 4019−4047.

(7) Zhu, Y.; Zhou, W.; Sunarso, J.; Zhong, Y.; Shao, Z. Phosphorus-Doped Perovskite Oxide as Highly Efficient Water Oxidation Electrocatalyst in Alkaline Solution. *Adv. Funct. Mater.* **2016**, *26*, 5862−5872.

(8) Royer, S.; Duprez, D.; Can, F.; Courtois, X.; Batiot-Dupeyrat, C.; Laassiri, S.; Alamdari, H. Perovskites as Substitutes of Noble Metals for Heterogeneous Catalysis: Dream or Reality. *Chem. Rev.* **2014**, *114*, 10292−10368.

(9) Hwang, J.; Rao, R. R.; Giordano, L.; Katayama, Y.; Yu, Y.; Shao-Horn, Y. Perovskites in Catalysis and Electrocatalysis. *Science* **2017**, *358*, 751−756.

(10) Keimer, B.; Kivelson, S. A.; Norman, M. R.; Uchida, S.; Zaanen, J. From Quantum Matter to High-Temperature Superconductivity in Copper Oxides. *Nature* **2015**, *518*, 179−186.

(11) Dagotto, E.; Hotta, T.; Moreo, A. Colossal Magnetoresistant Materials: The Key Role of Phase Separation. *Phys. Rep.* **2001**, *344*, 1−153.
(12) Salamon, M. B.; Jaime, M. The Physics of Manganites: Structure and Transport. *Rev. Mod. Phys.* **2001**, *73*, 583−628.
(13) Suntivich, J.; May, K. J.; Gasteiger, H. A.; Goodenough, J. B.; Shao-Horn, Y. A Perovskite Oxide Optimized for Oxygen Evolution Catalysis from Molecular Orbital Principles. *Science* **2011**, *334*, 1383−1385.
(14) Suntivich, J.; Gasteiger, H. A.; Yabuuchi, N.; Nakanishi, H.; Goodenough, J. B.; Shao-Horn, Y. Design Principles for Oxygen-Reduction Activity on Perovskite Oxide Catalysts for Fuel Cells and Metal-Air Batteries. *Nat. Chem.* **2011**, *3*, 546−550.
(15) Calle-Vallejo, F.; Inoglu, N. G.; Su, H.-Y.; Martínez, J. I.; Man, I. C.; Koper, M. T. M.; Kitchin, J. R.; Rossmeisl, J. Number of Outer Electrons as Descriptor for Adsorption Processes on Transition Metals and Their Oxides. *Chem. Sci.* **2013**, *4*, 1245−1249.
(16) Retuerto, M.; Pascual, L.; Piqué, O.; Kayser, P.; Salam, M. A.; Mokhtar, M.; Alonso, J. A.; Peña, M.; Calle-Vallejo, F.; Rojas, S. How Oxidation State and Lattice Distortion Influence the Oxygen Evolution Activity in Acid of Iridium Double Perovskites. *J. Mater. Chem. A* **2021**, *9*, 2980−2990.
(17) Grimaud, A.; May, K. J.; Carlton, C. E.; Lee, Y.-L.; Risch, M.; Hong, W. T.; Zhou, J.; Shao-Horn, Y. Double Perovskites as a Family of Highly Active Catalysts for Oxygen Evolution in Alkaline Solution. *Nat. Commun.* **2013**, *4*, 2439.
(18) Yagi, S.; Yamada, I.; Tsukasaki, H.; Seno, A.; Murakami, M.; Fujii, H.; Chen, H.; Umezawa, N.; Abe, H.; Nishiyama, N.; Mori, S. Covalency-Reinforced Oxygen Evolution Reaction Catalyst. *Nat. Commun.* **2015**, *6*, 8249.
(19) Yamada, I. Novel Catalytic Properties of Quadruple Perovskites. *Sci. Technol. Adv. Mater.* **2017**, *18*, 541−548.
(20) Yamada, I.; Fujii, H.; Takamatsu, A.; Ikeno, H.; Wada, K.; Tsukasaki, H.; Kawaguchi, S.; Mori, S.; Yagi, S. Bifunctional Oxygen Reaction Catalysis of Quadruple Manganese Perovskites. *Adv. Mater.* **2017**, *29*, No. 1603004.
(21) Guan, D.; Zhou, J.; Hu, Z.; Zhou, W.; Xu, X.; Zhong, Y.; Liu, B.; Chen, Y.; Xu, M.; Lin, H.-J.; Chen, C.-T.; Wang, J.-Q.; Shao, Z. Searching General Sufficient-and-Necessary Conditions for Ultrafast Hydrogen-Evolving Electrocatalysis. *Adv. Funct. Mater.* **2019**, *29*, No. 1900704.
(22) Zhu, M.; Guan, D.; Hu, Z.; Lin, H.-J.; Chen, C.-T.; Sheu, H.-S.; Wang, S.; Zhou, J.; Zhou, W.; Shao, Z. Synergistic Effects in Ordered Co Oxides for Boosting Catalytic Activity in Advanced Oxidation Processes. *Appl. Catal. B: Environ.* **2021**, *297*, No. 120463.
(23) Tjeng, L. H.; Chen, C. T.; Cheong, S. W. Comparative Soft-X-Ray Resonant-Photoemission Study on $Bi_2Sr_2CaCu_2O_8$, CuO, and $Cu_2O$. *Phys. Rev. B* **1992**, *45*, 8205−8208.
(24) Ye, X.; Liu, Z.; Wang, W.; Hu, Z.; Lin, H.-J.; Weng, S.-C.; Chen, C.-T.; Yu, R.; Tjeng, L.-H.; Long, Y. High-Pressure Synthesis and Spin Glass Behavior of a Mn/Ir Disordered Quadruple Perovskite $CaCu_3Mn_2Ir_2O_{12}$. *J. Phys.: Condens. Matter* **2020**, *32*, No. 075701.
(25) Deng, H.; Liu, M.; Dai, J.; Hu, Z.; Kuo, C.; Yin, Y.; Yang, J.; Wang, X.; Zhao, Q.; Xu, Y.; Fu, Z.; Cai, J.; Guo, H.; Jin, K.; Pi, T.; Soo, Y.; Zhou, G.; Cheng, J.; Chen, K.; Ohresser, P.; Yang, Y.-F.; Jin, C.; Tjeng, L.-H.; Long, Y. Strong Enhancement of Spin Ordering by a-Site Magnetic Ions in the Ferrimagnet $CaCu_3Fe_2Os_2O_{12}$. *Phys. Rev. B* **2016**, *94*, No. 024414.
(26) Dai, J.; Yin, Y.; Wang, X.; Shen, X.; Liu, Z.; Ye, X.; Cheng, J.; Jin, C.; Zhou, G.; Hu, Z.; Weng, S.; Wan, X.; Long, Y. Pentavalent Iridium Pyrochlore $Cd_2Ir_2O_7$: A Prototype Material System for Competing Crystalline Field and Spin-Orbit Coupling. *Phys. Rev. B* **2018**, *97*, No. 085103.
(27) Agrestini, S.; Chen, K.; Kuo, C. Y.; Zhao, L.; Lin, H. J.; Chen, C. T.; Rogalev, A.; Ohresser, P.; Chan, T. S.; Weng, S. C.; Auffermann, G.; Völzke, A.; Komarek, A. C.; Yamaura, K.; Haverkort, M. W.; Hu, Z.; Tjeng, L. H. Nature of the Magnetism of Iridium in the Double Perovskite $Sr_2CoIrO_6$. *Phys. Rev. B* **2019**, *100*, No. 014443.
(28) Chen, J.; Wang, X.; Hu, Z.; Tjeng, L. H.; Agrestini, S.; Valvidares, M.; Chen, K.; Nataf, L.; Baudelet, F.; Nagao, M.; Inaguma, Y.; Belik, A. A.; Tsujimoto, Y.; Matsushita, Y.; Kolodiazhnyi, T.; Sereika, R.; Tanaka, M.; Yamaura, K. Enhanced Magnetization of the Highest-$T_C$ Ferrimagnetic Oxide $Sr_2CrOsO_6$. *Phys. Rev. B* **2020**, *102*, No. 184418.
(29) Cheng, J. G.; Zhou, J. S.; Yang, Y. F.; Zhou, H. D.; Matsubayashi, K.; Uwatoko, Y.; MacDonald, A.; Goodenough, J. B. Possible Kondo Physics near a Metal-Insulator Crossover in the A-Site Ordered Perovskite $CaCu_3Ir_4O_{12}$. *Phys. Rev. Lett.* **2013**, *111*, No. 176403.
(30) Meyers, D.; Middey, S.; Cheng, J. G.; Mukherjee, S.; Gray, B. A.; Cao, Y.; Zhou, J. S.; Goodenough, J. B.; Choi, Y.; Haskel, D.; Freeland, J. W.; Saha-Dasgupta, T.; Chakhalian, J. Competition between Heavy Fermion and Kondo Interaction in Isoelectronic a-Site-Ordered Perovskites. *Nat. Commun.* **2014**, *5*, 5818.
(31) Li, X.; Wang, H.; Cui, Z.; Li, Y.; Xin, S.; Zhou, J.; Long, Y.; Jin, C.; Goodenough, J. B. Exceptional Oxygen Evolution Reactivities on $CaCoO_3$ and $SrCoO_3$. *Sci. Adv.* **2019**, *5*, No. eaav6262.
(32) Zhao, G.; Li, P.; Cheng, N.; Dou, S. X.; Sun, W. An Ir/Ni(OH)(2) Heterostructured Electrocatalyst for the Oxygen Evolution Reaction: Breaking the Scaling Relation, Stabilizing Iridium(V), and Beyond. *Adv. Mater.* **2020**, *32*, No. 2000872.
(33) Gao, R.; Zhang, Q.; Chen, H.; Chu, X.; Li, G.-D.; Zou, X. Efficient Acidic Oxygen Evolution Reaction Electrocatalyzed by Iridium-Based 12L-Perovskites Comprising Trinuclear Face -Shared $IrO_6$ Octahedral Strings. *J. Energy Chem.* **2020**, *47*, 291−298.
(34) Seitz, L. C.; Dickens, C. F.; Nishio, K.; Hikita, Y.; Montoya, J.; Doyle, A.; Kirk, C.; Vojvodic, A.; Hwang, H. Y.; Norskov, J. K.; Jaramillo, T. F. A Highly Active and Stable $IrO_x/SrIrO_3$ Catalyst for the Oxygen Evolution Reaction. *Science* **2016**, *353*, 1011−1014.
(35) Luo, Q.; Lin, D.; Zhan, W.; Zhang, W.; Tang, L.; Luo, J.; Gao, Z.; Jiang, P.; Wang, M.; Hao, L.; Tang, K. Hexagonal Perovskite $Ba_{0.9}Sr_{0.1}Co_{0.8}Fe_{0.1}Ir_{0.1}O_{3-\delta}$ as an Efficient Electrocatalyst towards the Oxygen Evolution Reaction. *ACS Appl. Energy Mater.* **2020**, *3*, 7149−7158.
(36) McCrory, C. C. L.; Jung, S.; Peters, J. C.; Jaramillo, T. F. Benchmarking Heterogeneous Electrocatalysts for the Oxygen Evolution Reaction. *J. Am. Chem. Soc.* **2013**, *135*, 16977−16987.
(37) Wu, Y.; Sun, W.; Zhou, Z.; Zaman, W. Q.; Tariq, M.; Cao, L.; Yang, J. Highly Efficient Oxygen Evolution Activity of $Ca_2IrO_4$ in an Acidic Environment due to Its Crystal Configuration. *ACS Omega* **2018**, *3*, 2902−2908.
(38) Bo, X.; Li, Y.; Chen, X.; Zhao, C. Operando Raman Spectroscopy Reveals Cr-Induced-Phase Reconstruction of NiFe and CoFe Oxyhydroxides for Enhanced Electrocatalytic Water Oxidation. *Chem. Mater.* **2020**, *32*, 4303−4311.
(39) Weng, B.; Xu, F.; Wang, C.; Meng, W.; Grice, C. R.; Yan, Y. A layered $Na_{1-x}Ni_yFe_{1-y}O_2$ double oxide oxygen evolution reaction electrocatalyst for highly efficient water-splitting. *Energy Environ. Sci.* **2017**, *10*, 121−128.
(40) Dionigi, F.; Zeng, Z.; Sinev, I.; Merzdorf, T.; Deshpande, S.; Lopez, M. B.; Kunze, S.; Zegkinoglou, I.; Sarodnik, H.; Fan, D.; Bergmann, A.; Drnec, J.; de Araujo, J. F.; Gliech, M.; Teschner, D.; Zhu, J.; Li, W.-X.; Greeley, J.; Cuenya, B. R.; Strasser, P. In-situ structure and catalytic mechanism of NiFe and CoFe layered double hydroxides during oxygen evolution. *Nat. Commun.* **2020**, *11*, 2522.
(41) Zhai, P.; Xia, M.; Wu, Y.; Zhang, G.; Gao, J.; Zhang, B.; Cao, S.; Zhang, Y.; Li, Z.; Fan, Z.; Wang, C.; Zhang, X.; Miller, J. T.; Sun, L.; Hou, J. Engineering single-atomic ruthenium catalytic sites on defective nickel-iron layered double hydroxide for overall water splitting. *Nat. Commun.* **2021**, *12*, 4587.
(42) Yamada, I.; Takamatsu, A.; Asai, K.; Ohzuku, H.; Shirakawa, T.; Uchimura, T.; Kawaguchi, S.; Tsukasaki, H.; Mori, S.; Wada, K.; Ikeno, H.; Yagi, S. Synergistically Enhanced Oxygen Evolution Reaction Catalysis for Multielement Transition-Metal Oxides. *ACS Appl. Energy Mater.* **2018**, *1*, 3711−3721.


https://doi.org/10.1021/acs.chemmater.1c03015
*Chem. Mater.* 2021, 33, 9295−9305

(43) Yagi, S.; Wada, K.; Yuuki, J.; Liu, W.; Yamada, I. Effects of Size and Crystallinity of $CaCu_3Fe_4O_{12}$ on Catalytic Activity for Oxygen Evolution Reaction. *Mater. Trans.* **2020**, *61*, 1698−1702.
(44) Yang, L.; Yu, G.; Ai, X.; Yan, W.; Duan, H.; Chen, W.; Li, X.; Wang, T.; Zhang, C.; Huang, X.; Chen, J.-S.; Zou, X. Efficient oxygen evolution electrocatalysis in acid by a perovskite with face-sharing $IrO_6$ octahedral dimers. *Nat. Commun.* **2018**, *9*, 5236.
(45) Sun, H.; Song, S.; Xu, X.; Dai, J.; Yu, J.; Zhou, W.; Shao, Z.; Jung, W. Recent Progress on Structurally Ordered Materials for Electrocatalysis. *Adv. Energy Mater.* **2021**, *11*, No. 2101937.
(46) Pi, Y. C.; Xu, Y.; Li, L. G.; Sun, T.; Huang, B. L.; Bu, L. Z.; Ma, Y. H.; Hu, Z. W.; Pao, C. W.; Huang, X. Q. Selective Surface Reconstruction of a Defective Iridium-Based Catalyst for High-Efficiency Water Splitting. *Adv. Funct. Mater.* **2020**, *30*, No. 2004375.
(47) Zhang, L.; Jang, H.; Liu, H.; Kim, M. G.; Yang, D.; Liu, S.; Liu, X.; Cho, J. Sodium-Decorated Amorphous/Crystalline $RuO_2$ with Rich Oxygen Vacancies: A Robust pH-Universal Oxygen Evolution Electrocatalyst. *Angew. Chem. Int. Ed.* **2021**, *60*, 18821−18829.
(48) Qin, Q.; Jang, H.; Wang, Y.; Zhang, L.; Li, Z.; Kim, M. G.; Liu, S.; Liu, X.; Cho, J. Gettering La Effect from $La_3IrO_7$ as a Highly Efficient Electrocatalyst for Oxygen Evolution Reaction in Acid Media. *Adv. Energy Mater.* **2021**, *11*, No. 2003561.
(49) Wu, H.; Zhang, B.; Liang, H.; Zhai, L.; Wang, G.; Qin, Y. Distance Effect of Ni-Pt Dual Sites for Active Hydrogen Transfer in Tandem Reaction. *Innovation (N.Y.)* **2020**, *1*, No. 100029.
(50) Grimaud, A.; Demortière, A.; Saubanère, M.; Dachraoui, W.; Duchamp, M.; Doublet, M.-L.; Tarascon, J.-M. Activation of Surface Oxygen Sites on an Iridium-Based Model Catalyst for the Oxygen Evolution Reaction. *Nat. Energy* **2017**, *2*, 16189.
(51) Shi, L.; Chen, H.; Liang, X.; Liu, Y.; Zou, X. Theoretical Insights into Nonprecious Oxygen-Evolution Active Sites in Ti-Ir-Based Perovskite Solid Solution Electrocatalysts. *J. Mater. Chem. A* **2020**, *8*, 218−223.
(52) Bajdich, M.; García-Mota, M.; Vojvodic, A.; Nørskov, J. K.; Bell, A. T. Theoretical Investigation of the Activity of Cobalt Oxides for the Electrochemical Oxidation of Water. *J. Am. Chem. Soc.* **2013**, *135*, 13521−13530.
(53) Manna, K.; Sarkar, R.; Fuchs, S.; Onykiienko, Y. A.; Bera, A. K.; Cansever, G. A.; Kamusella, S.; Maljuk, A.; Blum, C. G. F.; Corredor, L. T.; Wolter, A. U. B.; Yusuf, S. M.; Frontzek, M.; Keller, L.; Iakovleva, M.; Vavilova, E.; Grafe, H. J.; Kataev, V.; Klauss, H. H.; Inosov, D. S.; Wurmehl, S.; Büchner, B. Noncollinear Antiferromagnetism of Coupled Spins and Pseudospins in the Double Perovskite $La_2CuIrO_6$. *Phys. Rev. B* **2016**, *94*, No. 144437.
(54) Kim, S.-W.; Liu, C.; Kim, H.-J.; Lee, J.-H.; Yao, Y.; Ho, K.-M.; Cho, J.-H. Nature of the Insulating Ground State of the 5*d* Postperovskite $CaIrO_3$. *Phys. Rev. Lett.* **2015**, *115*, No. 096401.
(55) Sala, M. M.; Ohgushi, K.; Al-Zein, A.; Hirata, Y.; Monaco, G.; Krisch, M. $CaIrO_3$: A Spin-Orbit Mott Insulator Beyond the $j_{eff} = 1/2$ Ground State. *Phys. Rev. Lett.* **2014**, *112*, No. 176402.
(56) Hirose, K.; Fujita, Y. Clapeyron Slope of the Post-Perovskite Phase Transition in $CaIrO_3$. *Geophys. Res. Lett.* **2005**, *32*, No. L13313.
(57) Ohgushi, K.; Yamaura, J.-I.; Ohsumi, H.; Sugimoto, K.; Takeshita, S.; Tokuda, A.; Takagi, H.; Takata, M.; Arima, T.-H. Resonant X-ray Diffraction Study of the Strongly Spin-Orbit-Coupled Mott Insulator $CaIrO_3$. *Phys. Rev. Lett.* **2013**, *110*, No. 217212.
(58) Zhao, X.; Zhang, H. T.; Yan, Y.; Cao, J. H.; Li, X. Q.; Zhou, S. M.; Peng, Z. M.; Zeng, J. Engineering the Electrical Conductivity of Lamellar Silver-Doped Cobalt(II) Selenide Nanobelts for Enhanced Oxygen Evolution. *Angew. Chem. Int. Ed.* **2017**, *56*, 328−332.
(59) Shang, C.; Cao, C.; Yu, D.; Yan, Y.; Lin, Y.; Li, H.; Zheng, T.; Yan, X.; Yu, W.; Zhou, S.; Zeng, J. Electron Correlations Engineer Catalytic Activity of Pyrochlore Iridates for Acidic Water Oxidation. *Adv. Mater.* **2018**, *31*, No. 1805104.
(60) Zhao, Q.; Liu, M.; Dai, J.; Deng, H.; Yin, Y.; Zhou, L.; Yang, J.; Hu, Z.; Agrestini, S.; Chen, K.; Pellegrin, E.; Valvidares, M.; Nataf, L.; Baudelet, F.; Tjeng, L. H.; Yang, Y. F.; Jin, C.; Long, Y. High-Pressure Synthesis and Ferrimagnetic Ordering of the B-Site-Ordered Cubic Perovskite $Pb_2FeOsO_6$. *Inorg. Chem.* **2016**, *55*, 9816−9821.
(61) Meetei, O. N.; Erten, O.; Randeria, M.; Trivedi, N.; Woodward, P. Theory of High $T_c$ Ferrimagnetism in a Multiorbital Mott Insulator. *Phys. Rev. Lett.* **2013**, *110*, No. 087203.
(62) Goodenough, J. B., *Magnetism and the Chemical Bond*; Interscience Publishers: New York-London, 1963, 165−190.
(63) Hou, Y. S.; Xiang, H. J.; Gong, X. G. Lattice-distortion Induced Magnetic Transition from Low-temperature Antiferromagnetism to High-temperature Ferrimagnetism in Double Perovskites $A_2FeOsO_6$ (A = Ca, Sr). *Sci. Rep.* **2015**, *5*, 13159.
(64) Larson, A. C.; Dreele, R. B. V. *General Structure Analysis System (GSAS)*. Los Alamos National Laboratory Report LAUR 2004, 86−784.
(65) Kresse, G.; Furthmüller, J. Efficient Iterative Schemes for Ab Initio Total-Energy Calculations Using a Plane-Wave Basis Set. *Phys. Rev. B* **1996**, *54*, 11169−11186.
(66) Kresse, G.; Joubert, D. From Ultrasoft Pseudopotentials to the Projector Augmented-Wave Method. *Phys. Rev. B* **1999**, *59*, 1758−1775.
(67) Perdew, J. P.; Burke, K.; Ernzerhof, M. Generalized Gradient Approximation Made Simple. *Phys. Rev. Lett.* **1996**, *77*, 3865−3868.
(68) Dudarev, S. L.; Botton, G. A.; Savrasov, S. Y.; Humphreys, C. J.; Sutton, A. P. Electron-Energy-Loss Spectra and the Structural Stability of Nickel Oxide: An LSDA+U Study. *Phys. Rev. B* **1998**, *57*, 1505−1509.
(69) Tang, R.; Nie, Y.; Kawasaki, J. K.; Kuo, D.-Y.; Petretto, G.; Hautier, G.; Rignanese, G.-M.; Shen, K. M.; Schlom, D. G.; Suntivich, J. Oxygen Evolution Reaction Electrocatalysis on $SrIrO_3$ Grown Using Molecular Beam Epitaxy. *J. Mater. Chem. A* **2016**, *4*, 6831−6836.
(70) Monkhorst, H. J.; Pack, J. D. Special Points for Brillouin-Zone Integrations. *Phys. Rev. B* **1976**, *13*, 5188−5192.


https://doi.org/10.1021/acs.chemmater.1c03015
*Chem. Mater.* 2021, 33, 9295−9305